FUSION OF MULTI-TEMPORAL AND MULTI-SENSOR ICE VELOCITY OBSERVATIONS

Laurane Charrier[1,2,*], Yajing Yan[1], Elise Colin Koeniguer[2], Jeremie Mouginot[3], Romain Millan[3,4], Emmanuel Trouvé[1]

[1] Université Savoie Mont Blanc, LISTIC, Annecy France
[2] ONERA, DTIS, Paris, France,
[3] IGE, Université Grenoble Alpes, Grenoble, France,
[4] Department of Geosciences and Natural Resource Management, University of Copenhagen, Copenhagen K, Denmark

Commission 3, WG III/9

KEY WORDS: velocity time series, multi-sensors, multi-temporal, fusion, glacier displacements

ABSTRACT:

Ice velocity observations available on-line or on-demand at intra-annual resolution still contain gaps, noise, and artifacts, especially in mountain areas. There is a need to fuse the available multi-temporal and multi-sensor velocity observations to be able to study intra-annual glacier dynamics. The proposed approach includes an inversion based on the temporal closure of displacement observation networks and a temporal interpolation. It reconstructs velocity time series between consecutive dates at a regular temporal sampling (called Regular Leap Frog (RLF) time series) inferred from all the velocity observations without a prori knowledge on the displacement behavior. The RLF time series can be reconstructed for different temporal sampling. Root Mean Square Error (RMSE) over stable areas and Velocity Vector Coherence (VVC) over fast moving areas are proposed to select a temporal sampling allowing a compromise between uncertainty and temporal resolution. This study focuses on the Fox glacier, in the Southern Alps of New Zealand. It shows that RMSE over stable areas is decreased from 78% for a temporal sampling of 5 days to 40% for a temporal sampling of 60 days. Thus, using this approach, we obtain a velocity time series with a complete temporal coverage and reduced uncertainty for a regular and optimal temporal sampling. The results highlight the large seasonal variability of the flow of Fox Glacier that fluctuates by more than 30% between spring and autumn.

1. INTRODUCTION

The increasing amount of remote sensing images enables the estimation of glacier velocities with a temporal resolution up to 2 days and a sampling resolution up to 50 m all over the world (Millan et al., 2019). While numerous ice velocity observations are available on-line (Gardner et al., 2018, Fahnestock et al., 2016, Millan et al., 2019, Friedl et al., 2018), this large amount of data is still difficult to analyze, since velocity observations span different temporal baselines, have variable sampling resolution and are derived from different sensors. Velocities obtained from a small temporal baseline are close to the derivative of the displacement but are more likely to be contaminated by noise uncorrelated in time. Velocities obtained from a long temporal baseline approximate the mean velocity between two dates but can be affected by large errors due to temporal decorrelation. Despite of filtering steps, ice velocity observations produced by automated processing chains contain gaps, noise, and artifacts, especially in mountain areas where image-matching algorithms are more likely to fail because of surface locking, shadow casting, feature-less regions or strong surface changes (Dehecq et al., 2019, Altena and Kääb, 2020). In order to take advantage of the available dense velocity observations for the study of intra-annual glacier dynamics, there is a need to develop advanced post-processing methods to fuse the available multi-temporal and multi-sensor velocity observations.

To carry out a regression on displacement observations from different temporal baselines, (Greene et al., 2020) propose to integrate over the time a parametric regression function. However, it requires a priori knowledge of the displacement beha-

vior. Another approach to fuse velocities with different temporal baselines and to reduce the uncertainty is the temporal closure of the displacement observation network. This approach was originally developed for Interferometric Synthetic-Aperture Radar (InSAR) time series and called Small BAseline Subset (SBAS) approach (Berardino et al., 2002, Lanari et al., 2007, López-Quiroz et al., 2009). The SBAS approach uses interferograms produced by image pairs spanning small temporal and geometrical baselines to minimize temporal and geometrical decorrelation. Later, this approach has been applied to offset-tracking displacement measurement of SAR images (Casu et al., 2011, Euillades et al., 2016, Guo et al., 2020, Charrier et al., 2021a, Charrier et al., 2021b) and optical images (Bontemps et al., 2018, Lacroix et al., 2019, Ding et al., 2020).

However, most of the authors who use the temporal closure approach consider only one sensor (Altena et al., 2019, López-Quiroz et al., 2009, Casu et al., 2011, Berardino et al., 2002, López-Quiroz et al., 2009, Euillades et al., 2016, Charrier et al., 2021a, Charrier et al., 2021b) or invert a time series from each sensor apart (Kim et al., 2015, Ding et al., 2020). Only a few studies choose to include datasets from different sensors in one inversion. (Pepe et al., 2016) proposes to invert displacement time series from ASAR/ENVISAT and CSK velocity observations. Since the two datasets are not overlapping in time, they add a constrain based on a displacement model to solve the system. Besides, (Bontemps et al., 2018) include displacements from different Spot and Pléiade images to invert displacements between consecutive observed dates.

Both previous studies open perspectives to take advantage of

---

* Corresponding author: laurane.charrier@univ-smb.fr

multi-sensors datasets. However, methodological or pratical issues still exist, for example, the use of a model-based constrain in (Pepe et al., 2016) requires a priori knowledge of the displacement behavior. In addition, the inversion of displacements between consecutive observed dates as done in (Bontemps et al., 2018) is problematic for fast moving target such as glaciers since it produces irregular time series, i.e., the displacements are inverted between dates which are not equally distributed over the period. Indeed, (Bontemps et al., 2018) are interested in cumulative displacement (CD) time series, i.e. displacements between each date and a reference date, to study slow moving landslide whereas velocities between consecutive dates, named Leap Frog (LF) velocity time series in (Hadhri et al., 2019, Charrier et al., 2021b), are more appropriate to analyze intra-annual variations of fast moving targets such as glaciers (Greene et al., 2020, Derkacheva et al., 2020). The analysis of an irregular LF time series can raise issues because: 1) The resulted velocities does not have the same temporal sampling. Since velocities measured on different temporal samplings are representative of the average displacement on different time intervals, LF displacements are not truly comparable if the temporal sampling of the LF time series is irregular. 2) displacements with very short temporal sampling are inverted if the images from the different sensors are acquired a few days apart (for example up to 1 day apart between Venµs and Sentinel-2 satellites). However, very short temporal sampling velocities are likely to be more noisy (Casu et al., 2011, Millan et al., 2019, Charrier et al., 2021b). 3) the dates between which the displacements are inverted can be different from one pixel to another because of different data quality since outliers are rejected in most of the available datasets (Millan et al., 2019, Gardner et al., 2018, Fahnestock et al., 2016).

Therefore, this paper aims at fusing velocity observations from different temporal baselines and sensors to obtain a LF time series with a regular and optimal temporal sampling to study intra-annual variations of ice velocity. For that, an Irregular LF (ILF) time series is first inverted. Then, a temporal interpolation is performed on a CD time series built by summing the ILF displacements. From the discrete derivative of this interpolated CD time series, a Regular LF (RLF) time series with an optimal temporal sampling is obtained. This temporal sampling is selected based on a compromise between uncertainty and temporal resolution. This approach is applied to Sentinel-2 and Venµs velocity observations covering the Fox glacier, in the Southern Alps of New Zealand.

2. DATA AND STUDY AREA

The study area is the Fox glacier which is situated in the Southern Alps of New Zealand. It is a fast-flowing, temporal maritime glacier (Purdie et al., 2008, Kääb et al., 2016).

The considered dataset is from (Millan et al., 2019). It contains velocity observations based on images acquired by two different optical sensors: Sentinel-2 and Venµs. The repeat cycles of the two satellites are 5 days and 2 days respectively and the spatial sampling of the images are 10 m and 5 m respectively. The radiometric resolution of the sensors are 12 and 10 bit. Displacement offsets are computed using a modified version of the cross-correlation algorithm *Ampcor* from NASA (Michel and Rignot, 1999). Post-processing have already been carried out to remove outliers: pixel offsets that deviate more than three pixels from a 9×9 pixels spatial median have been removed (Millan et al., 2019, Mouginot et al., 2012). The temporal baselines of the
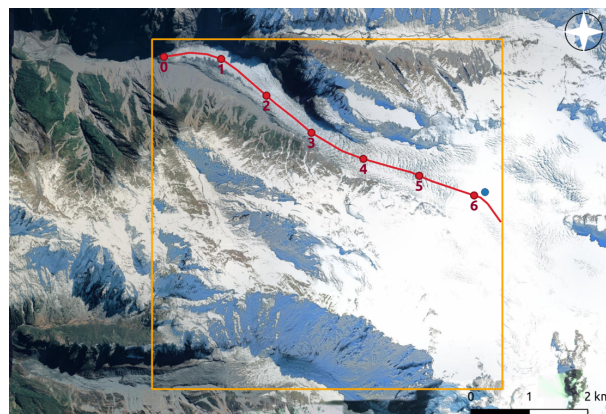

Figure 1. Studied area over the Fox glacier in the Southern Alps of New Zealand. The blue point is used for analysis in section 4. The orange rectangle corresponds to the considered area in section 4. The red longitudinal profile is considered for the spatio-temporal analysis in section 5. The red dotes are spaced 1 km apart. The background image is an optical image from the Google Earth collection.

velocity observations are ranging from 5 to 100 days and from 330 to 400 days. The resulting velocity fields are representing on the same spatial grid which have a 50 m spatial sampling, for both Venµs and Sentinel-2 velocities. The measurements cover a period from August 2016 to May 2019.

Figure 2 shows that Sentinel-2 velocities range from August 2016 to September 2018 whereas Venµs velocities range from January 2018 to May 2019. The percentage of non-masked velocities is on average 27% for Sentinel-2 and 14% for Venµs per central date and temporal baseline. This is due to outliers removal during post-processing. It highlights the difficulty to compute displacements on this narrow and fast glacier tongue and the need for a data fusion.
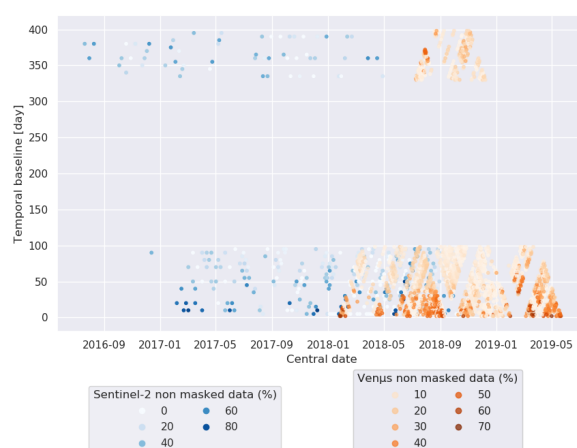

Figure 2. Temporal baselines of the velocity observations according to their central date for Sentinel-2 velocities in blue and Venµs velocities in orange. The colormap which ranges from light to dark blue or orange indicates the percentage of non masked data for each temporal baseline and central date.

2.1 Confidence values

In order to quantify the quality of velocity observations, a confidence value is computed for each velocity vector (2 components in x and y directions) as a combination of the following criteria:

1) the cosinus of the angle between each vector and the spatio-temporal median vector (Burgess et al., 2012, Nguyen et al., 2018) called Median Angle (MA) here and defined as:

$$\cos(\vec{u}_{i,j,t}, \vec{v}^w_{i,j}) = \frac{\vec{u}_{i,j,t} \cdot \vec{v}^w_{i,j}}{\|\vec{u}_{i,j,t}\| \|\vec{v}^w_{i,j}\|} \qquad (1)$$

where $u_{i,j,t}$ is the displacement vector at the pixel (i,j) and time t and $v^w_{i,j}$ is the median vector over the time on a spatial window w, here set to 3×3 pixels. If the two vectors are co-linear, as expected, this criterion will have a value of 1. The negative values are set to 0 to penalize vectors which have a direction from $90°$ to $180°$ away from the median direction.

2) the modified z-score which is a standardized and robust score that measures outlier strength (Maronna et al., 2019). The modified z-score is computed for the x and y component of the velocity vector as:

$$\text{MZscore} = \frac{x_{i,j,t} - \tilde{x}^w_{i,j}}{1.483 \, \text{MAD}} \qquad (2)$$

where $x_{i,j,t}$ stands for the x or y component of the velocity at the pixel (i,j) and time t, $\tilde{x}^w_{i,j}$ is the median of the x or y component of the velocity over the time on a spatial window w, here set to 3×3 pixels. MAD is the Median Absolute Deviation defined as: $\text{median}|x_{i,j,t} - \tilde{x}^w_{i,j}|$.

The final confidence value of two velocity components is the same for a given pixel and time stamp. It corresponds to the multiplication of the three criterion scaled between 0 and 1: the scaled modified z-score for x components of the velocity, the scaled modified z-score for y components of the velocity and the MA.

3. METHOD

3.1 Temporal inversion

To fuse multi-temporal and multi-sensor ice velocity observations, a temporal inversion based on the temporal closure of the displacement observation network is used. The key principle relies on making use of the redundancy of the displacement observation network to build a LF displacement time series that respects the temporal closure constraint. The temporal closure is formulated on a pixel-by-pixel basis on the set of n displacement observations d_{t_i,t_j} with a temporal baseline $t_j - t_i$ contained in the vector Y. The temporal closure formulation is $Y = AX$ where X represents the vector of p output displacements $\hat{d}_{t_n,t_m}$ with a temporal sampling $t_m - t_n$, and A is a design matrix of dimension $n \times p$ linking X with Y.

The proposed method is an extension of (Charrier et al., 2021a) and (Charrier et al., 2021b). In (Charrier et al., 2021b), the mono-sensor dataset had enough redundancy to obtain directly a regular time series at user-defined temporal sampling using an improved temporal closure formulation. However, in the case
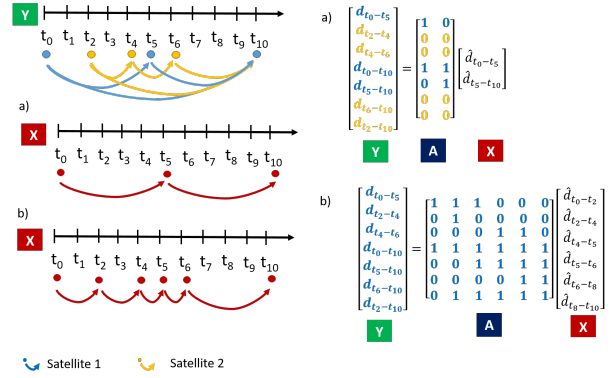

Figure 3. Illustration of the temporal closure of the displacement observation network used to obtain a) a regular LF time series. The temporal sampling corresponds to the Satellite 1 repeat cycle b) an Irregular LF time series. The vector Y corresponds to the displacement observations. The vector X stands for the LF displacement time series. A is the design matrix linked X and Y in the temporal closure.

of a multi-sensor data set with numerous gaps, the problem is more complex.

As shown in Figure 3 a), if X is a time series with the same temporal sampling as the satellite 2, the displacements from the satellite 1 could not be included in the system $AX = Y$ because it is not possible to write d_{t_2,t_4}, d_{t_4,t_6}, $d_{t_6,t_{10}}$ and $d_{t_2,t_{10}}$ as a linear combination of $\hat{d}_{t_0,t_5}$ and $\hat{d}_{t_5,t_{10}}$. Hence, the design matrix A contains four rows of zero, the system is ill posed and some information is lost.

Therefore, a solution can be to invert an irregular time series of displacements between each date of the displacement observations Y, as illustrated in Figure 3 b) to include all the observations in the system.

The system $AX = Y$ is then solved using an Iterative Re-weighted Least Square inversion with a regularization term on the discrete derivative of the leap frog velocities, as described in (Charrier et al., 2021b, Charrier et al., 2021a). The a priori weight corresponds to the confidence values presented in section 2.1. The result of the inversion gives an Irregular LF (ILF) time series.

3.2 Interpolation

In the ILF time series, each velocity $\hat{v}_{t_m,t_n}$ corresponds to a given temporal sampling $t_m - t_n$. The velocities are not truly comparable if the temporal sampling is different because velocities measured on a small time interval are close to the derivative of the displacement whereas velocities measured on long time interval approximate the mean velocity between two dates. Therefore, an interpolation of this time series would not be rigorous. Hence, the interpolation should be done on Cumulative Displacement time series. The latest is built by summation of the ILF displacements obtained after inversion as:

$$\hat{d}_{t_0,t_k} = \sum_{0}^{k-\Delta\tau_k} \hat{d}_{t_m,t_{m+\Delta\tau_m}} \qquad (3)$$

with $\hat{d}_{t_0,t_k}$ a CD displacement between dates t_0 and t_k, $\hat{d}_{t_m,t_{m+\Delta\tau_m}}$ a LF displacement between dates t_m and $t_{m+\Delta\tau_m}$, $\Delta\tau_m$ the temporal sampling of the LF displacement m.
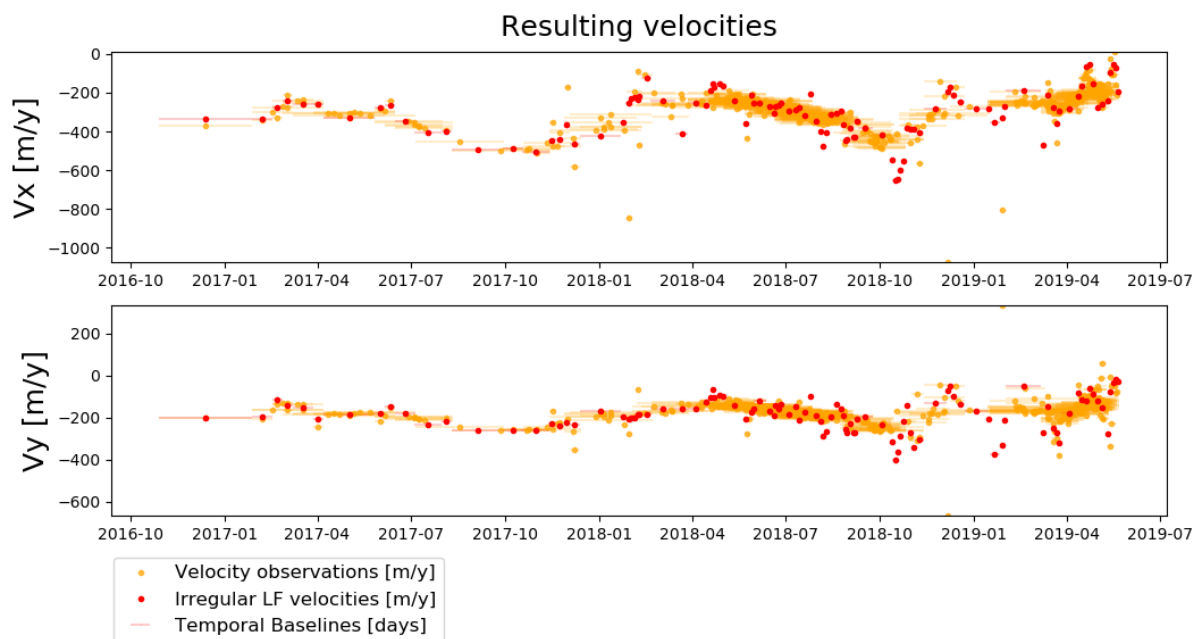
Figure 4. Velocity observations in gold overlayed with the Irregular Leap Frog time series obtained after temporal inversion in red for the point of coordinates (-43.532,170.134) labeled as the blue point in Figure 1.

Then, the CD time series is interpolated using a cubic interpolation. Finally, a Regular LF time series is recovered by using a discrete derivative of the interpolated CD time series:

$$\hat{d}_{t_r,t_{r+\Delta\tau_r}} = \hat{d}_{t_0,t_{r+\Delta\tau_r}} - \hat{d}_{t_0,t_r} \qquad (4)$$

where $\hat{d}_{t_r,t_{r+\Delta\tau_r}}$ is a LF displacement between dates t_r and $t_{r+\Delta\tau_r}$. $\Delta\tau_r$ is the temporal sampling, which is identical for all the displacements in the time-series.

This discrete derivative can be computed at different temporal samplings. The choice of the temporal sampling will be discussed in section 4.2.

4. REGULAR LEAP FROG TIME SERIES WITH AN OPTIMAL TEMPORAL BASELINE

4.1 Irregular LF time series

The temporal inversion of multi-sensor velocities results in an Irregular LF time series. An example is shown on Figure 4 for the point of coordinates (-43.532,170.134), corresponding to the the blue point on Figure 1. The ILF displacements are coherent with the velocity observations trend. However, the results look noisy especially after January 2018 where Sentinel-2 and Venµs observations are overlapping. Because of this overlap, the time interval between two observations is small, i.e. up to 1 day. Therefore, the temporal samplings of the ILF time series are also small. Velocity is obtained by dividing displacement by the time, hence if each displacement has a constant white noise due to image correlation errors (Millan et al., 2019, Mouginot et al., 2012), the noise of small temporal baseline velocities could be larger than the velocity magnitude.

Figure 5 shows the distribution of temporal samplings according to their central date over the area represented in orange on Figure 1. It reveals the heterogeneity of temporal baselines
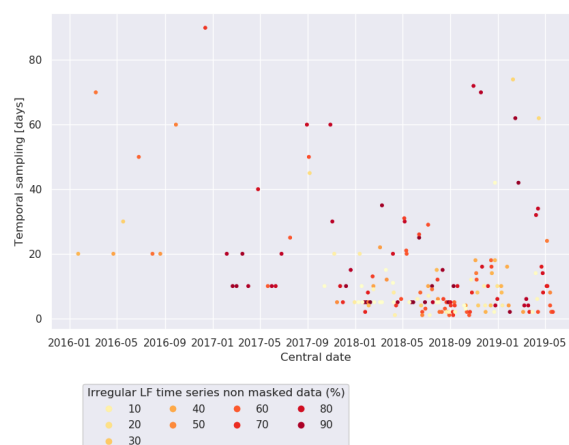

Figure 5. Temporal baselines of the Irregular Leap Frog time series according to their central date. The colormap indicates the percentage of non masked data for each temporal baseline and central date.

which ranges from 1 to 90 days with a median value of 8 days. The smallest temporal baselines are recorded after January 2018 where Sentinel-2 and Venµs observations are overlapped. Moreover, the ILF displacements are inverted between the dates of the available observations for each pixel. Because of the previous outlier removal, these dates differ from one pixel to another. This implies that the velocity values of a given central date and temporal baselines are not reconstructed for every pixel. The percentage of non-masked value is 52% in average. This highlights the necessity to homogenize the temporal sampling of the ILF time series to facilitate the interpretation of the results.
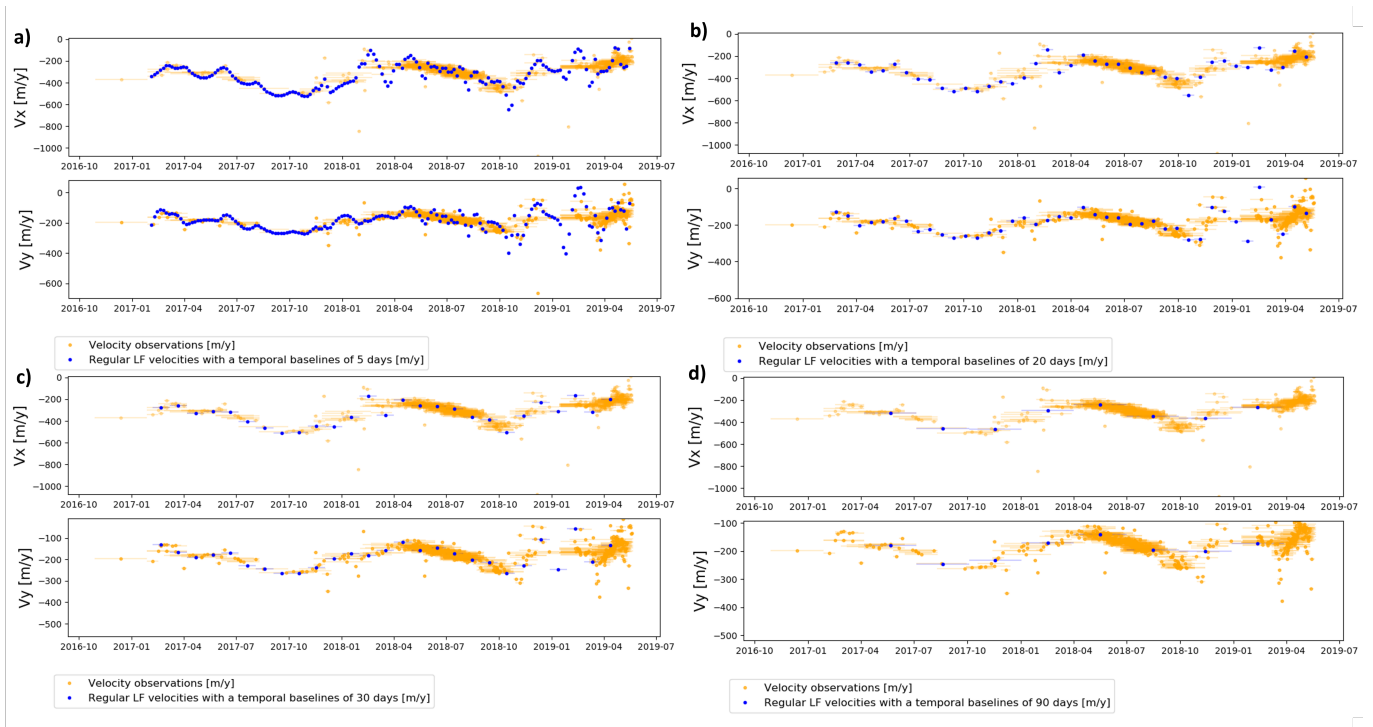
Figure 6. Velocity observations (in gold) overlayed with the RLF time series in blue for the point of coordinates (-43.532,170.134) labeled as the blue point in Figure 1. The RLF time series have a temporal sampling of a) 5 days b) 20 days c) 30 days and d) 90 days.

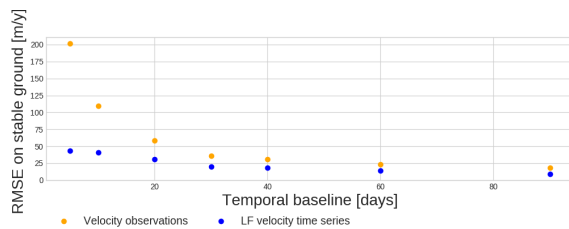## 4.2 Regular LF time series with different temporal sampling

Figure 7. Comparison of RMSE over stable areas for different temporal samplings. RMSE is performed over ice-free areas according to the Randolph Glacier Inventory V6.0.
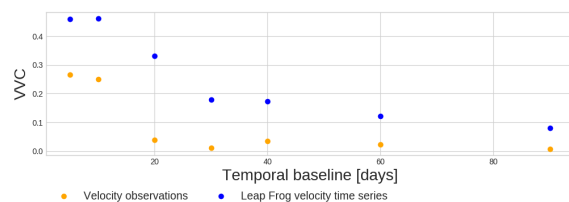

Figure 8. Comparison of VVC over fast moving ice for different temporal samplings. VVC is computed on glaciers areas according to the Randolph Glacier Inventory V6.0 where the mean velocity magnitude observation is higher than 400 m/y.

After interpolation of the CD time series, a Regular LF time series can be reconstructed with any temporal sampling. A question arises: how to choose the optimal temporal sampling to study the short-term variation of ice velocity with an optimal signal-to-noise ratio?

It can be seen on Figure 6 that the larger is the temporal sampling, the smoother is the RLF time series. There is less noise but also a smaller temporal resolution. For example, the 5-day RLF presented on Figure 6a) is robust to the main outliers (e.g. vx=-900 m/y in February 2018 or vy=-650m/y in December 2018) but record very abrupt velocity variations (e.g between October 2018 and February 2019). Because the spline interpolation fit every points of the CD time series, the smallest is the temporal sampling of the RLF, the highest is the risk to overfit the data.

To characterize the uncertainty of the RLF time series according to their temporal sampling, two criterion are defined:

1) the Root Mean Square Error (RMSE) over stable areas which relies on the assumption that the velocity magnitude is null on the stable areas. It is defined as:

$$\text{RMSE} = \text{mean}_{(i,j) \in \omega_1} \sqrt{\frac{1}{N+1} \sum_{t=0}^{N} \left\| \vec{v}(i,j,t) \right\|^2} \quad (5)$$

where $\vec{v}(i,j,t)$ stands for the velocity vector at time t and pixel (i,j), $N+1$ is the number of velocity data at pixel (i,j) over the considered period, ω_1 corresponds to ice-free areas defined according to the Randolph Glacier Inventory (RGI) V6.0 (RGI-Consortium et al., 2017).

2) the Velocity Vector Coherence (VVC) metric (Dehecq et al., 2015, Nguyen et al., 2018) over fast moving areas which relies on the assumption that the flow direction on a point is roughly stable in time. It is a defined as:

$$\text{VVC} = \text{mean}_{(i,j) \in \omega_2} \left\| \sum_{t=0}^{N} \frac{\vec{V}(i,j,t)}{\|\vec{V}(i,j,t)\|} \right\| \quad (6)$$

where ω_2 corresponds to the glacier parts where the mean of velocity observation magnitude is higher than 400 m/y.

These two criterion are computed for several temporal baselines on the area symbolized in orange on Figure 1.

Figure 7 shows that whatever is the temporal baseline/sampling, the RMSE over stable areas is always lower for the RLF time series than for the velocity observations: from 78% lower for a temporal baseline of 5 days to 40% lower for a temporal baseline of 60 days. In addition, Figure 8 highlights that VVC is lower for the velocity observations than for the RLF time series than for every temporal baselines: from 94% higher for a temporal baseline of 30 days to 42% higher for a temporal baseline of 5 days.

Moreover, the largest is the temporal baseline, the lowest is the RMSE and the highest is the VVC, i.e., the lowest is the uncertainty. The RMSE and VVC values reach a plateau at a temporal baseline of 40 days corresponding to a RMSE of 31 m/y for the velocity observations, and at temporal baseline of 30 days corresponding to a RMSE of 20 m/y for the RLF time series. This analysis provides a way to select an optimal temporal baseline/sampling which allows a compromise between temporal resolution and uncertainty. Since the RMSE and VVC of the RLF time series are roughly stable after a temporal sampling of 30 days, 30-days can be selected as an optimal temporal sampling. The RMSE and VVC of the velocity observations are stable after 40 days, the optimal temporal baselines would be 40 days. Hence, the optimal temporal sampling and the associated uncertainty is smaller for RLF time series than for the velocity observations.

5. SPATIO-TEMPORAL ANALYSIS OF THE RESULTS

Figure 9 b) shows the temporal evolution of the RLF time series at a temporal sampling of 30 days along a longitudinal profile represented on Figure 1. These results are compared with the initial velocity observations. To have a fair comparison, a moving average is performed using a temporal window of 30 days on the velocity observations. That is to say, for each period of 30 days, the average of all the velocities which overlap this period is computed. This post-processed dataset does not correspond to rough dataset and it is already a way to fuse data from different sensors and temporal baselines.

Figure 9 a) reveals that there is no velocity observations available in the center of the tongue between May and October 2017, between February and April 2018 and between October and November 2019. There are gaps in the dataset which make difficult the analysis of intra-annual variations of velocity. Using the proposed approach helps to fill in the gaps and decrease the uncertainty by using the temporal closure of the observation network and a temporal interpolation. Even if the method is pixel-based, the RLF time series seems to be spatially coherent: there is a smooth trend between pixels through the period. A seasonal signal is visible since ice velocity magnitude peaks between September and November and reaches a minimum between April and June. Along the longitudinal profile in Figure 9, the median increase between the minimum of velocity recorded in September to November 2017 and the maximum of velocity recorded from April to June 2018 is 40%. The median increase from April/June 2018 to September/November 2017 is 30%. Moreover, the RLF time series is coherent with

the moving averaged velocity observations. However, some discrepancies can be noticed: for instance, the velocity magnitudes at 2.6 km in 2018 range between 200 and 800 m/y whereas the surrounding pixels show velocity magnitudes between 800 and 1200 m/y. This may be due to a discrepancy in the velocity observations which is also visible in Figure 9 a) at 2.6 km. This does not have a glaciological meaning and looks like an artefact. These kinds of remaining artefacts could be removed using a spatio-temporal interpolation or a spatial smoothing. It opens the discussion for further improvement of the current approach.

6. CONCLUSIONS

This article presents a new approach to fuse ice velocity observations from different temporal baselines and sensors in order to study short-term variations of glacier flow without any a priori on the displacement behavior. The proposed method relies on an inversion based on the temporal closure of the displacement observation network similar to the SBAS approach.

SBAS-like approaches usually retrieve Cumulative Displacement time series (displacements between each date and a reference date) whereas for fast-moving targets with a strong seasonality such as temperate glaciers, Leap Frog velocities (velocities between consecutive dates) are more adequate. To obtain an easily interpretable time series, the LF time series should have a regular temporal sampling, i.e., all the inverted velocities should span the same time interval. However, if the dataset is based on different sensors, it is not possible to obtain directly the same Regular LF time series for each pixel, especially if outliers are removed beforehand. Moreover, the length of the RLF temporal sampling is a crucial parameter but rarely discussed in the literature.

Therefore, the proposed approach firstly built an Irregular Leap Frog time series and then interpolate it to obtain a Regular Leap Frog time series. It enables the user to obtain a RLF time series on a unique temporal basis for each pixel while decreasing the uncertainty of the observations. The application of this method to Sentinel-2 and Venµs velocities covering the Fox glacier in the Southern Alps of New Zealand reveals that the Root Mean Square Error over stable areas is decreased from 78% lower for a temporal baseline of 5 days to 40% lower for a temporal baseline of 60 days. The RMSE over stable areas and VVC over fast moving areas are proposed to select a temporal sampling allowing a compromise between signal-to-noise ratio and temporal resolution. Finally, the 30-days RLF time series reveal a strong seasonal variation of ice velocity: velocities differ by more than 30% from spring to autumn. This was not clearly visible in the observations. It highlights the interest of the method to obtain a velocity time series with a complete temporal coverage and a reduced uncertainty at an optimal temporal sampling by taking advantage of all multi-sensor and multi-temporal velocity observations.

This approach is not dataset dependent and could be applied to all kinds of available velocity observations. A following of this work will be to fuse velocities based on optical and SAR images by tacking into account the different geometry of acquisition of SAR and optical sensors inside the fusion step.
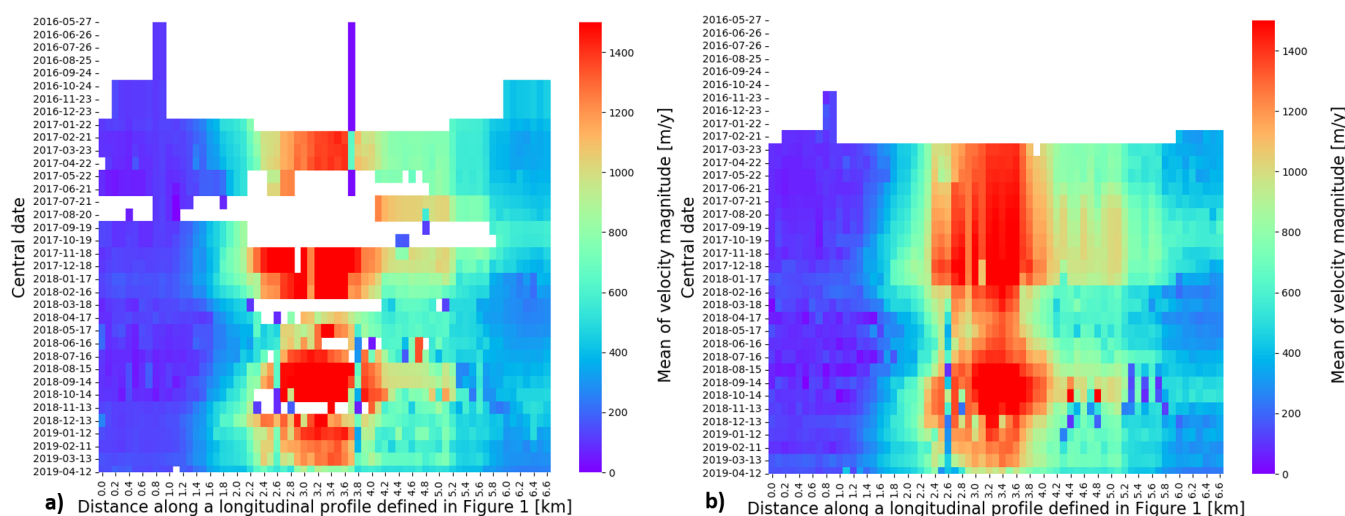
Figure 9. Color-encoded matrix of velocity magnitude according to the central date of the velocity and the distance along a longitudinal profile represented in red in Figure 1. This longitudinal profile goes from the terminus of the Fox glacier to the accumulation part, from the North-Est to the South-West. The color-encoded matrix stands for a) the 30-days moving average of velocity observations b) Regular Leap Frog velocity time series with a temporal sampling of 30 days.

REFERENCES

Altena, B., Kääb, A., 2020. Ensemble matching of repeat satellite images applied to measure fast-changing ice flow, verified with mountain climber trajectories on Khumbu icefall, Mount Everest. *Journal of Glaciology*, 66(260), 905–915.

Altena, B., Scambos, T. A., Fahnestock, M., Kääb, A., 2019. Extracting recent short-term glacier velocity evolution over southern Alaska and the Yukon from a large collection of Landsat data. *The Cryosphere*, 13(3), 795–814.

Berardino, P., Fornaro, G., Lanari, R., Sansosti, E., 2002. A new algorithm for surface deformation monitoring based on small baseline differential SAR interferograms. *IEEE Transactions on geoscience and remote sensing*, 40(11), 2375–2383.

Bontemps, N., Lacroix, P., Doin, M.-P., 2018. Inversion of deformation fields time-series from optical images, and application to the long term kinematics of slow-moving landslides in Peru. *Remote Sensing of Environment*, 210, 144–158.

Burgess, E., Forster, R., Larsen, C., Braun, M., 2012. Surge dynamics on Bering Glacier, Alaska, in 2008–2011. *The Cryosphere*, 6(6), 1251–1262.

Casu, F., Manconi, A., Pepe, A., Lanari, R., 2011. Deformation time-series generation in areas characterized by large displacement dynamics: The SAR amplitude pixel-offset SBAS technique. *IEEE Transactions on Geoscience and Remote Sensing*, 49(7), 2752–2763.

Charrier, L., Yan, Y., Colin-Koeniguer, E., Trouvé, E., 2021a. Fusion of glacier displacement observations with different temporal baselines. *2021 IEEE International Geoscience and Remote Sensing Symposium IGARSS*, IEEE, 5497–5500.

Charrier, L., Yan, Y., Koeniguer, E. C., Leinss, S., Trouvé, E., 2021b. Extraction of velocity time series with an optimal temporal sampling from displacement observation networks. *IEEE Transactions on Geoscience and Remote Sensing*, 1–1.

Dehecq, A., Gourmelen, N., Gardner, A. S., Brun, F., Goldberg, D., Nienow, P. W., Berthier, E., Vincent, C., Wagnon, P., Trouvé, E., 2019. Twenty-first century glacier slowdown driven by mass loss in High Mountain Asia. *Nature Geoscience*, 12(1), 22–27.

Dehecq, A., Gourmelen, N., Trouvé, E., 2015. Deriving large-scale glacier velocities from a complete satellite archive: Application to the Pamir–Karakoram–Himalaya. *Remote Sensing of Environment*, 162, 55–66.

Derkacheva, A., Mouginot, J., Millan, R., Maier, N., Gillet-Chaulet, F., 2020. Data Reduction Using Statistical and Regression Approaches for Ice Velocity Derived by Landsat-8, Sentinel-1 and Sentinel-2. *Remote Sensing*, 12(12), 1935.

Ding, C., Zhang, L., Liao, M., Feng, G., Dong, J., Ao, M., Yu, Y., 2020. Quantifying the spatio-temporal patterns of dune migration near Minqin Oasis in northwestern China with time series of Landsat-8 and Sentinel-2 observations. *Remote Sensing of Environment*, 236, 111498.

Euillades, L. D., Euillades, P. A., Riveros, N. C., Masiokas, M. H., Ruiz, L., Pitte, P., Elefante, S., Casu, F., Balbarani, S., 2016. Detection of glaciers displacement time-series using SAR. *Remote sensing of Environment*, 184, 188–198.

Fahnestock, M., Scambos, T., Moon, T., Gardner, A., Haran, T., Klinger, M., 2016. Rapid large-area mapping of ice flow using Landsat 8. *Remote Sensing of Environment*, 185, 84–94.

Friedl, P., Seehaus, T. C., Wendt, A., Braun, M. H., Höppner, K., 2018. Recent dynamic changes on Fleming glacier after the disintegration of Wordie ice shelf, Antarctic peninsula. *The Cryosphere*, 12(4), 1347–1365.

Gardner, A. S., Moholdt, G., Scambos, T., Fahnstock, M., Ligtenberg, S., Van Den Broeke, M., Nilsson, J., 2018. Increased West Antarctic and unchanged East Antarctic ice discharge over the last 7 years. *Cryosphere*, 12(2), 521–547.

Greene, C. A., Gardner, A. S., Andrews, L. C., 2020. Detecting seasonal ice dynamics in satellite images. *The Cryosphere*, 14(12), 4365–4378.

Guo, L., Li, J., Li, Z.-w., Wu, L.-x., Li, X., Hu, J., Li, H.-l., Li, H.-y., Miao, Z.-l., Li, Z.-q., 2020. The Surge of the Hispar Glacier, Central Karakoram: SAR 3-D Flow Velocity Time Series and Thickness Changes. *Journal of Geophysical Research: Solid Earth*, 125(7), e2019JB018945.

Hadhri, H., Vernier, F., Atto, A. M., Trouvé, E., 2019. Time-lapse optical flow regularization for geophysical complex phenomena monitoring. *ISPRS Journal of Photogrammetry and Remote Sensing*, 150, 135–156.

Kääb, A., Winsvold, S. H., Altena, B., Nuth, C., Nagler, T., Wuite, J., 2016. Glacier remote sensing using Sentinel-2. part I: Radiometric and geometric performance, and application to ice velocity. *Remote Sensing*, 8(7), 598.

Kim, J.-W., Lu, Z., Jia, Y., Shum, C., 2015. Ground subsidence in Tucson, Arizona, monitored by time-series analysis using multi-sensor InSAR datasets from 1993 to 2011. *ISPRS Journal of Photogrammetry and Remote Sensing*, 107, 126–141.

Lacroix, P., Araujo, G., Hollingsworth, J., Taipe, E., 2019. Self-Entrainment Motion of a Slow-Moving Landslide Inferred From Landsat-8 Time Series. *Journal of Geophysical Research: Earth Surface*, 124(5), 1201–1216.

Lanari, R., Casu, F., Manzo, M., Zeni, G., Berardino, P., Manunta, M., Pepe, A., 2007. An overview of the small baseline subset algorithm: A dinsar technique for surface deformation analysis. *Deformation and Gravity Change: Indicators of Isostasy, Tectonics, Volcanism, and Climate Change*, Springer, 637–661.

López-Quiroz, P., Doin, M.-P., Tupin, F., Briole, P., Nicolas, J.-M., 2009. Time series analysis of Mexico City subsidence constrained by radar interferometry. *Journal of Applied Geophysics*, 69(1), 1–15.

Maronna, R. A., Martin, R. D., Yohai, V. J., Salibián-Barrera, M., 2019. *Robust statistics: theory and methods (with R)*. John Wiley & Sons.

Michel, R., Rignot, E., 1999. Flow of Glaciar Moreno, Argentina, from repeat-pass Shuttle Imaging Radar images: comparison of the phase correlation method with radar interferometry. *Journal of Glaciology*, 45(149), 93–100.

Millan, R., Mouginot, J., Rabatel, A., Jeong, S., Cusicanqui, D., Derkacheva, A., Chekki, M., 2019. Mapping Surface Flow Velocity of Glaciers at Regional Scale Using a Multiple Sensors Approach. *Remote Sensing*, 11(21), 2498.

Mouginot, J., Scheuchl, B., Rignot, E., 2012. Mapping of ice motion in Antarctica using synthetic-aperture radar data. *Remote Sensing*, 4(9), 2753–2767.

Nguyen, T., Méger, N., Rigotti, C., Pothier, C., Trouvé, E., Gourmelen, N., Mugnier, J.-L., 2018. A Pattern-Based Method For Handling Confidence Measures While Mining Satellite Displacement Field Time Series: Application to Greenland Ice Sheet and Alpine Glaciers. *IEEE Journal of Selected Topics in Applied Earth Observations and Remote Sensing*, 11(11), 4390–4402.

Pepe, A., Bonano, M., Zhao, Q., Yang, T., Wang, H., 2016. The use of C-/X-band time-gapped SAR data and geotechnical models for the study of Shanghai's ocean-reclaimed lands through the SBAS-DInSAR technique. *Remote Sensing*, 8(11), 911.

Purdie, H., Brook, M., Fuller, I., 2008. Seasonal variation in ablation and surface velocity on a temperate maritime glacier: Fox Glacier, New Zealand. *Arctic, Antarctic, and Alpine Research*, 40(1), 140–147.

RGIConsortium et al., 2017. Randolph Glacier Inventory–A dataset of global glacier outlines: Version 6.0. *Global Land Ice Measurements from Space, Colorado, USA, Tech. Rep.*